Landslide Experiments on Artificial and Natural Slopes

Hirotaka Ochiai* · **Toshiaki Sammori** · **Yasuhiko Okada**

Abstract. An almost real-size slope model was used to study the initiation process of landslide fluidization during torrential rain. Experiments were conducted by filling an inclined flume with loose sand under the rainfall simulator to induce the sand to collapse. Both the movement, volumetric strain and the pore water pressure of the sand were monitored throughout the experiments, from the start of spraying to the cessation of the landslide. These experiments showed: (*1*) Landslide fluidization caused by undrained rapid loading undergoes three stages: compaction of the sand layer by the sliding mass from upper slope, generation of excess pore water pressure in saturated zone, and induction of fast shearing; (*2*) Fluidization at the collapse source area undergoes also three stages: destruction and compaction of sand layer skeleton by outbreak of shearing, increase of pore water pressure in saturated zone, and shift to hi-speed shearing, these three stages take place almost simultaneously.

An experiment to induce a fluidized landslide by artificial rainfall was conducted on a natural slope at Mt. Kaba-san in Yamato village, Ibaraki Prefecture, Japan. The experimental slope was 30 m long, 5 m wide, and the average slope gradient was 33 degrees. A landslide initiated 24 627.5 s (410 min 27.5 s) after the start of sprinkling at a rainfall intensity of 78 mm hr^{-1}. The landslide mass was 14 m long and 1.2 m deep (at maximum). It first slid, then fluidized, and changed into a debris flow. The travel distance was up to 50 m in 17 seconds. The apparent friction angle of the fluidized landslide was 16.7 degrees. Formation of the sliding surface was detected by soil-strain probes. Motion of the surface of the failed landslide mass was determined by stereo photogrammetry.

Keywords. Landslide, fluidization, flume experiment, pore-water pressure, natural slope, sliding surface formation, stereo photogrammetry, soil surface movement

15.1 Introduction

Fluidized landslides, which travel long distances at high speed, are one of the most dangerous types of landslides (Sassa 2000). Fluidized slope movement takes place both in artificial cut slopes and natural slopes and often results in extensive property damage and significant loss of life (Sassa 1984, 1998). Many fluidized landslides have been observed in Japan, some of them have caused great disasters.

A debris flow that occurred in 1996 in Gamahara-zawa, Nagano, Japan, is an example of a fluidized landslide. The debris flow was triggered by the collapse at around 1 300 m in altitude, and moved approximately 39 000 m^3 of soil, of which 8 000 m^3 was deposited on the landslide section and 31 000 m^3 traveled down a slope 16.4° in mean inclination along a river for approximately 3 km. The debris flow eroded another 37 000 m^3 of soil, of which 15 000 m^3 was captured by an check dam. As a result, approximately 53 000 m^3 of soil reached the alluvial fan, which is 300 m in altitude, and 14 people were in the death by the debris flow (Committee Investigation for Gamahara-zawa Debris Flow Damage in Dec. 6, 1997). As this soil balance shows, the debris flow expanded the volume while traveling down the slope by gathering up river-bed sediment, and almost doubled in the amount of soil. Sassa (1998) called this phenomenon a landslide-induced debris flow. The fluidization of the river-bed sediment was caused by the rapid loading of the landslide and expanded moving mass led to the further fluidization of the lower part which increased the volume.

Liquefaction is an important mechanism in causing the fluidized motion of some landslides, where fluidization occurs along the sliding surface, or within the sliding zone during a rise in pore-water pressure which reduces shear resistance by decreasing the effective normal stress. Bishop (1973) noted that fluidization can be distinguished from general sliding, which usually has an intact soil mass above the sliding surface. Hutchinson (1986) noted that flow-like motion subsequent to fluidization is a neglected and little-understood group of movements with confusing terminology. Liquefaction phenomena as a result of cyclic loading have received much attention from many researchers since the drastic effects of liquefaction were noted after the 1964 Niigata earthquake Japan. Seed and Lee (1966), Yoshimi et al. (1977), Seed (1979), Ishihara et al. (1990) and (1993) discuss extensive laboratory soil tests attempting to reveal the liquefaction mechanism. Effects such as rainfall, as well as motion effects, can trigger fluidized landslides (Eckersley 1985, 1990; Sassa et al. 2004).

In order to reproduce a fluidized landslide at almost field scale, and to investigate its fluidization mechanisms, the National Research Center for Disaster Prevention, Tsukuba Japan, constructed an indoor rainfall simulator and large-scale flume model 10 m long, 4 m wide, and 1.2 m deep. By using such facilities, Fukuzono (1985) proposed that the initiation time of rainfall-induced slope failure was a function of inverse of shear velocity. Iverson and LaHusen (1989) pointed out that pore-water pressures within the soil packed

in the slope model were dynamically fluctuating during the rapid shearing at failure. These findings were obtained from indoor flume tests in which the soil sample was quasi-uniformly packed. Iverson et al. (2000) verified the effects of void ratio on initial landslide speed by ring shear tests and flume experiments. They showed that shearing of a soil layer in large void ratio caused a sudden rise in pore water pressure and flow failure. Whereas, in a case of smaller void ratio, pore water pressure was reduced, soil mass was separated into blocks, some of which slipped discontinuously, did not flow in flume experiments.

These studies reviewed above were concerning to the mechanism and conditions for flow failure generation. Several theories have been proposed in them, such as the undrained shear in loose soil layer, rearrangement of soil particle blocks near the shear surfaces and particle breakage causing soil contraction and excess pore water pressure. However, the contraction of soil layers has not been observed during actual landslides and is merely a conjecture supported by soil tests and model experiments. Our study aimed to reproduce the contraction of soil layers and the generation of excess pore water pressure, both of which have only been reproduced inside soil testers, in a real-size landslide model, and to prove the fluidization mechanisms of landslide masses.

Landslide experiments on natural slopes by sprinkling or water supplying from trenches have been reported four times in Japan and United States of America. The respective conditions for each experiment are shown in Table 15.1. In our study, we conducted a rainfall-induced landslide experiment on a natural slope which had more complex and heterogeneous characteristics than the indoor models, in an attempt to investigate the dynamic movements of the soil surface, the formation of the sliding surface, and hydrological characteristics, based on the results of the indoor flume testing. The experimental slope was 30 m long and 5 m wide, and mainly covered by weathered disintegrated granite sand. Soil-surface movements were monitored by using stereo photogrammetry. Hence white-coloured targets were placed on the experimental slopes and the movements of these targets were traced by image analysis. To detect the formation of the sliding surface, soil-strain probes were inserted into the soil to 2 m depth at deepest. Tensiometers were used to measure changes in pore-water pressures within the soil.

Table 15.1. Soil properties of the sand for the experiments

Dry density (surface)	γ_d	1.33 g cm^{-3}
Void ratio (surface)	e	0.73
Saturated water content	w_{sat}	32%
Internal friction angle	ϕ'	30.6°
Cohesion	c'	0.75 kPa
50% diameter of soil particle	D_{50}	0.51 mm
Silt + Clay content		0.6%
Uniformity coefficient	U_c	3.5
Coefficient of permiability	k	1.2×10^{-2} cm s^{-1}
Approximate mobility index	AMI	1.14

15.2 Landslide Fluidization Process by Flume Experiment

15.2.1 Experimental Flume

A schematic diagram of the experimental flume is shown in Fig. 15.1. Figure 15.2 shows the model flume before collapse. The sizes are shown in the Fig. 15.1. One side of the flume was covered by reinforced glass to observe

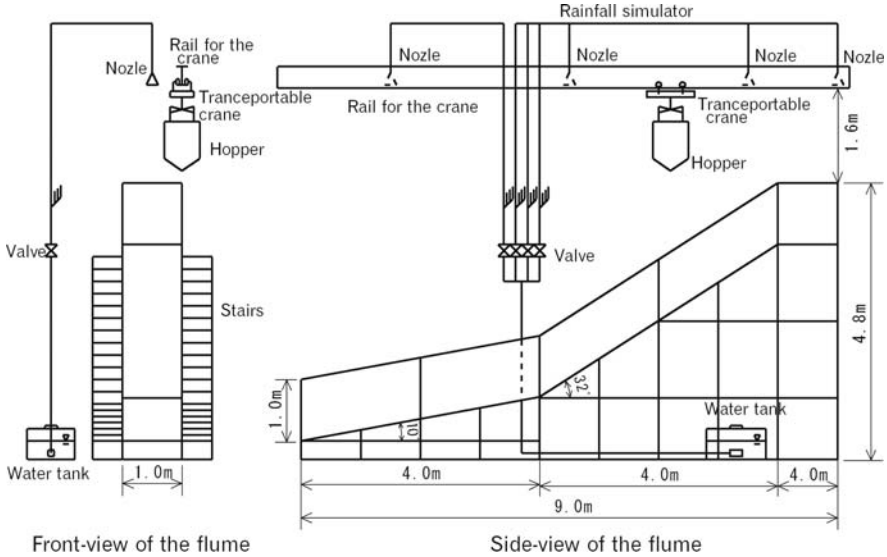

Fig. 15.1. The front-view and side-view of the flume. Rainfall simulator and the rail for transportable crane are equipped over the flume

sand movement. The inclination of the slope was different between the upper and lower sections to induce collapse at the upper part of the slope and observe how the collapsed soil induces new slide on the lower. Sand was loosely filled into the flume by gently dropping the sand from a mobile hopper.

The rain simulator was equipped with nozzles at four points all 6.4 m above the floor along the flume. For all experiments, rain intensity of 100 mm hr^{-1} was used.

15.2.2 Observation System

The concept of the observation system is illustrated in Fig. 15.3. The system was developed to simultaneously monitor the change in pore water pressure and sand movement. Synchrony of data was attempted by generating time codes from a time-code generator, recording the codes together with pore water pressure measurements, and displaying them in video camera images of the sand movement.

To measure dynamically fluctuating pore water pressure, a small cylindrical pressure transducer (8.3 cm long and 1.8 cm in diameter) was embedded within the sand. The transducer moved together with the sand but did not hinder the movement.

The movement of the sand was filmed with three video camera sets located along the glass side of the flume, which filmed the 2–4 m, 4–6 m, and 6–8 m lengthwise sections. The movements of several points within the sand layer were traced by burying cylinders of 3.0 cm in length and 1.6 cm in diameter within the sand so that one bottom side of each cylinder was adjacent and visible through the glass. The display of the time-code generator was placed along the flume so that the elapsed time codes were also filmed in the video camera images. The codes were also recorded in the data files of pore water pressure. Pore water pressure measurements were conducted at 100 Hz, and 30 video camera images were recorded per second.

Fig. 15.2. The flume before collapse

15.2.3 Sand Layer Shapes and Configuration of the Instruments

Four experiments were conducted by changing the thickness of the sand layer at the upper and lower slope sections. The thickness of the sand layer at the upper and lower slope sections was 0.5 m and 0.5 m in Experiment 1, 0.5 m and 0.7 m in Experiment 2, 0.7 m and 0.5 m in Experiment 3, and 0.7 m and 0.7 m in Experiment 4, respectively. Figure 15.4 shows the initial sand layer cross-sections and the positions of the instruments in Experiment 1. The properties of the sand used for the experiments were tested in advance.

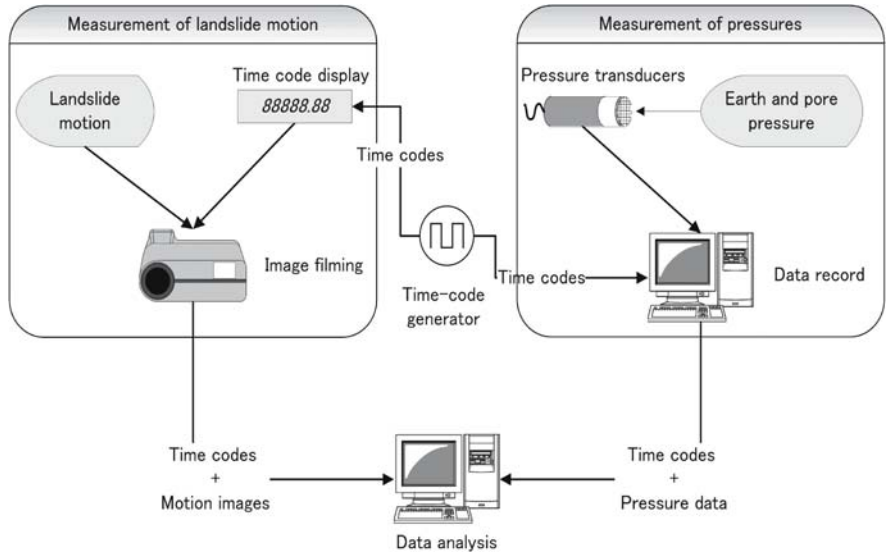

Fig. 15.3. The measurement system

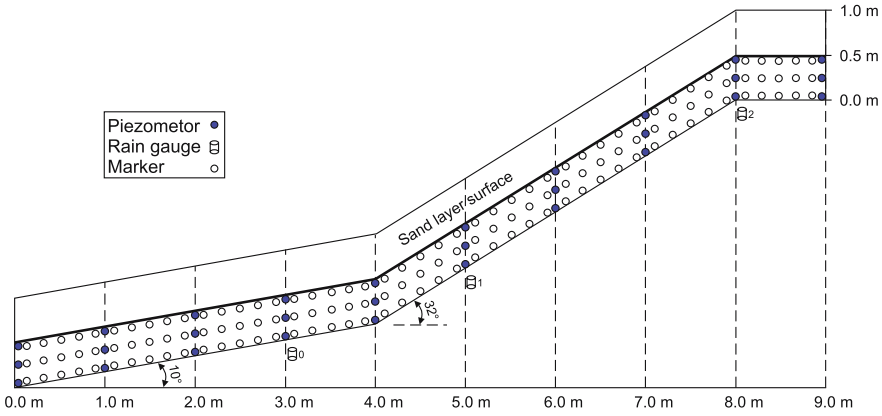

Fig. 15.4.
The side-view of sand layer and configuration of instruments in Experiment 1

Table 15.2. The thickness of sand layer, time of collapse initiation and mean water content in upper slope right before collapse in each example of experiment

Exp. No.	Upper slope thickness (m)	Lower slope thickness (m)	Accumulation amount of rainfall (mm)	Water content in upper slope (%)
1	0.5	0.5	81.5	27.1
2	0.5	0.7	72.2	26.1
3	0.7	0.5	108.2	27.3
4	0.7	0.7	111.2	27.3

15.2.4 Results and Discussion

15.2.4.1 Properties of the Sand Used for the Experiments

The same sand was used for all experiments. The results of soil tests are listed in Table 15.1. The internal friction angle φ' and cohesion c' were derived by direct shear tests. AMI values were determined with the following equation:

$$\mathrm{AMI} = \frac{w_{\mathrm{sat}}}{w_{\mathrm{L}}} \tag{15.1}$$

where, w_{sat} is the saturated water content and w_{L} is the liquid limit. According to Ellen and Fleming (1987), collapsed soil mass easily fluidizes when AMI > 1.0. Our sand sample satisfied AMI conditions of easily fluidizing soil.

15.2.4.2 Cumulative Rainfall until the Collapse

The thickness of the sand layers, the cumulative amount of rain, and the mean water content of the upper slope section are listed in Table 15.2 for each experiment. In all experiments, the sand layer collapsed from the upper section. The table shows that the cumulative amount of rain until the collapse and the thickness of the upper sand layer have a positive correlation. The wetting front travels vertically downward from the sand surface at a constant speed. When the wetting front reaches the bottom of the flume, the water forms a water table and destabilizes the slope. Therefore, there is a positive correlation between the thickness of the sand layer and the cumulative rainfall until the formation of the water table.

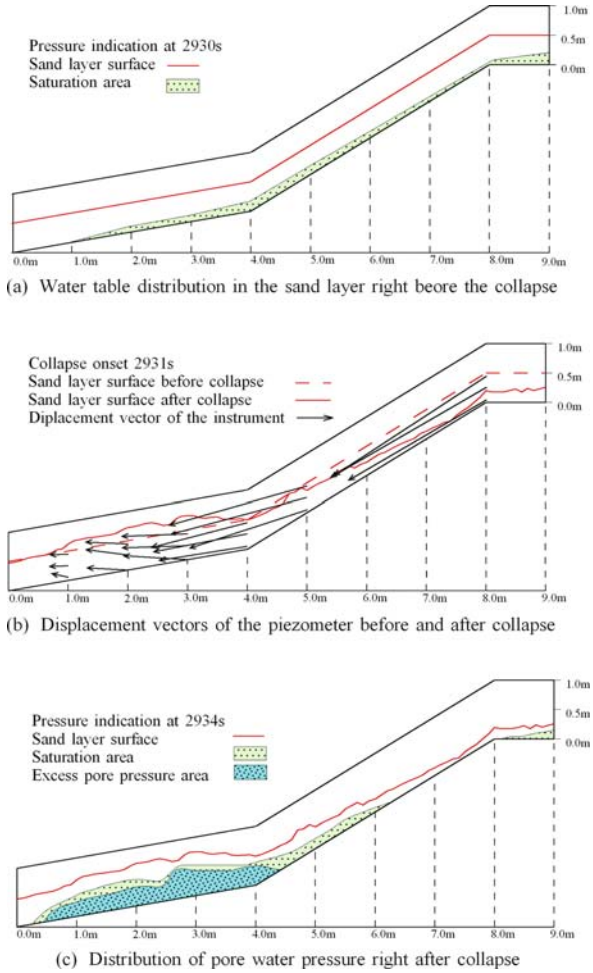

Fig. 15.5. The side view of the sand layer right before and after collapse in Experiment 1

15.2.4.3 Landslide Motion and Pore Water Pressure Distribution

Figures 15.5 to 15.8 show: (*a*) the water table within the sand layer immediately before the collapse; (*b*) the form of the sand layer surface and the displacement vector of the pressure transducer embedded within the sand before and after the collapse; and (*c*) the pore water pressure distribution within the sand layer immediately after the collapse and sedimentation, for Experiments 1 to 4.

Figure 15.5 shows the results of Experiment 1, which used uniform sand layer thickness of 0.5 m. As shown in Fi. 15.5a, the water table was uniformly distributed over the flume floor at both the upper and lower slope sections. Figure 15.5b shows that the slip surface was generated along the water table. As shown in Fig. 15.5c, the excess pore water pressure after the collapse was generated in a compressed sand section. Here, the section of excess pore water pressure is a section below the water table and showed water pressure values larger than estimated hydrostatic pressure.

Figure 15.6 is for Experiment 2, which was 0.5 m in sand thickness at the upper section and 0.7 m at the lower section. The water table was found only in the upper slope (Fig. 15.6a), and the wetting front did not reach the bottom of the flume at the lower section (Fig. 15.6b). Therefore, the slip surface was observed only in the upper slope section, and the excess pore water pressure was recorded in a compressed section near the border of the lower and upper sections (Fig. 15.6c).

On the other hand, Experiment 3 (Fig. 15.7) was 0.7 m at the upper section and 0.5 m at the lower section. The water table was far from the bottom at the lower section (Fig. 15.7a). Since the upper slope section was thicker than the lower section, a relatively heavy mass acted on the lower sand layer, and the traveling soil flowed over the wall at the lowest side of the flume. The excess pore water pressure was observed in the compressed section near the bottom side.

In Experiment 4 (Fig. 15.8), the thickness of the sand was 0.7 m throughout the flume. The water table was ob-

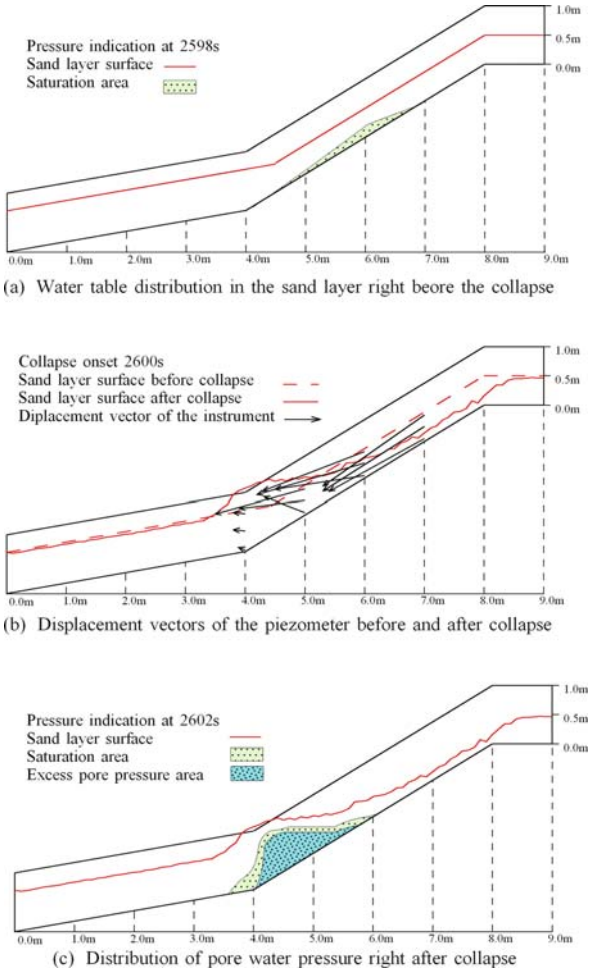

(a) Water table distribution in the sand layer right beore the collapse

(b) Displacement vectors of the piezometer before and after collapse

(c) Distribution of pore water pressure right after collapse

Fig. 15.6. The side view of the sand layer right before and after collapse in Experiment 2

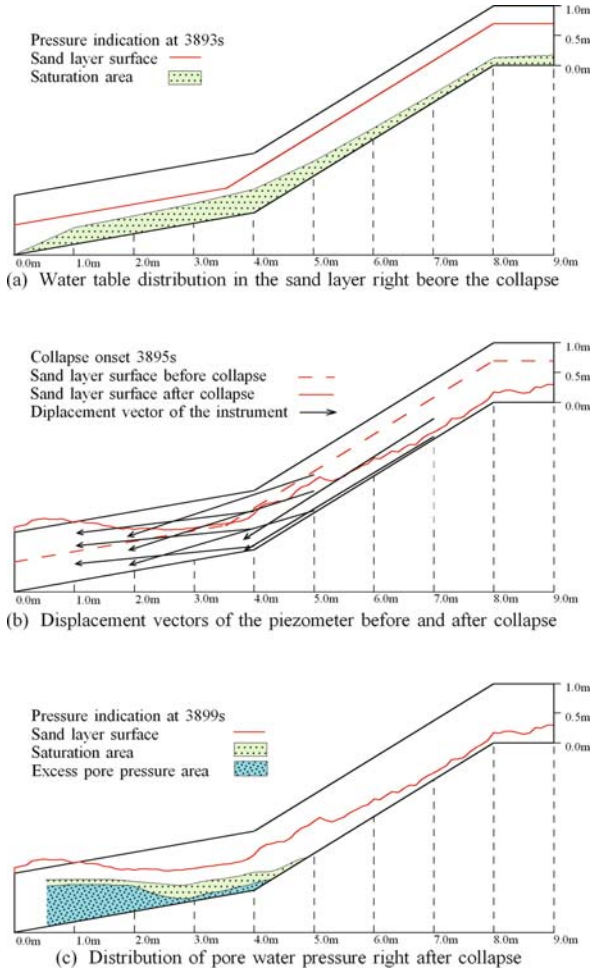

(a) Water table distribution in the sand layer right beore the collapse

(b) Displacement vectors of the piezometer before and after collapse

(c) Distribution of pore water pressure right after collapse

Fig. 15.7. The side view of the sand layer right before and after collapse in Experiment 3

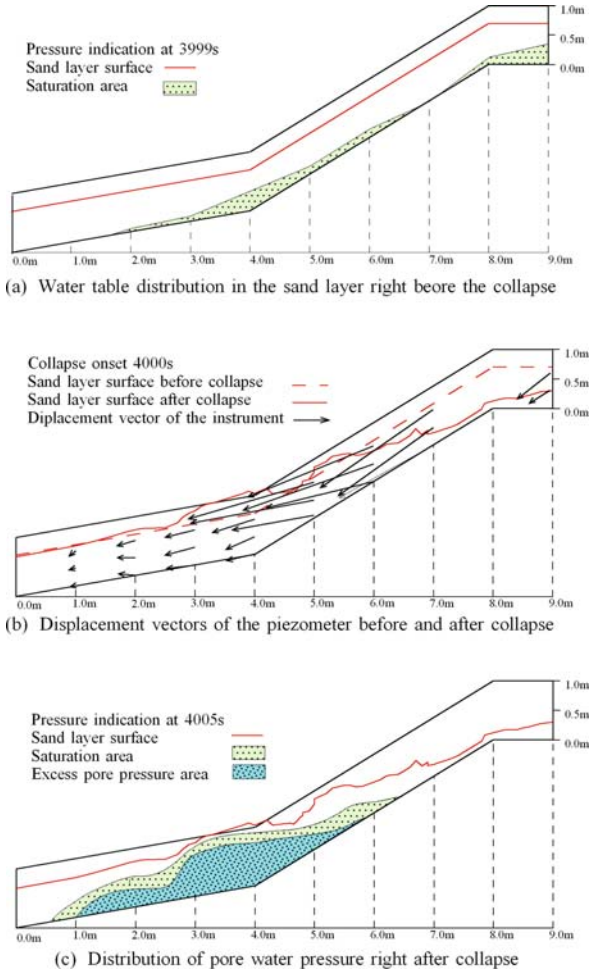

Fig. 15.8. The side view of the sand layer right before and after collapse in Experiment 4

served extending from the upper to the lower slope sections but not reaching the very lower section of 0–1.5 m (Fig. 15.8a). The water table was high near the point where the inclination changed. The collapse of the sand started at the upper slope section, and the moving mass applied undrained sudden load to and compressed the lower sections and induced the sections to slip (Fig. 15.8b). Compared to Fig. 15.5b, which shows horizontal compression of the lower sand section, Fig. 15.8b shows both horizontal and vertical compression of the sand.

Figures 15.5 to 15.8 show:

1. Collapse occurred at the upper slope sections. In all experiments other than Experiment 2, the collapsed sand mass compressed and induced the lower sections to slide.
2. Shearing occurred in sections in which water tables were formed immediately before the collapse.
3. Excess pore water pressure was generated in compressed sand sections.

15.2.4.4 Volumetric Strain, Velocity, and Pore Water Pressure Fluctuation

Figure 15.9 shows the speed of soil movement, volumetric strain, pore water pressure, and change in sand thickness all at the compressed soil section 3 m from the lowest end of the flume for Experiments 1 to 4. Volumetric strain and the speed of movement were determined from video camera images of the markers embedded in the sand. In all experiments, it was difficult to trace the markers as the landslide progressed, or to determine the volumetric strain and traveling speed.

As shown in the figure, in Experiment 1, the lower slope section received horizontal compression by the collapse of the upper slope. As soon as the semi-consolidated top section started to move, both the negative volumetric strain and head value increased at the 45 cm-deep section, or near the floor of the flume (2931.5 s). The head value exceeded the thickness of the sand layer, causing excess pore water, and induced rapid shearing even in the 45 cm-deep section (2932 s). The head value dropped once, but was restored by the thickening of the sand layer induced by the load of the falling mass. The undrained sudden loading condition was maintained, and the head value rose once more, which was 78 cm at the 45 cm-deep section when the sand layer was 60 cm thick (2932.8 s).

In Experiment 2, the sliding soil mass did not reach the lower slope, and we could not determine sand movement or measure the head values.

Experiment 3 showed processes similar to those in Experiment 1, but excess pore water pressures also at 5 cm- and 25 cm-deep sections, according to the sensors embedded in these sections. This was likely attributable to the water table being located near the surface immediately before the collapse and to liquefaction that was caused by rapid and turbulent sand movement. The head value at 45 cm deep jumped and then dropped (3895 s), but gradually increased thereafter along with the thickening of the sand layer. Along with the rapid rise in soil thickness while the landslide mass overrun the bottom wall, the head value increased steeply (3896.5 s). The head value was about 100 cm when the sand was 70 cm thick (3896.7 s).

Experiment 4 showed processes similar to those in Experiments 1 and 3. The head value was 125 cm when the overlying sand layer was 90 cm thick (4005 s).

These experimental analyses showed:

1. Fluidization that is caused by undrained sudden loading of landslide mass undergoes three stages: compaction of the sand layer by the collapse, generation of excess pore water pressure in saturated soil sections, and induction of rapid shearing.
2. Pore water pressure increases more rapidly in saturated area than in unsaturated through rapid compaction.

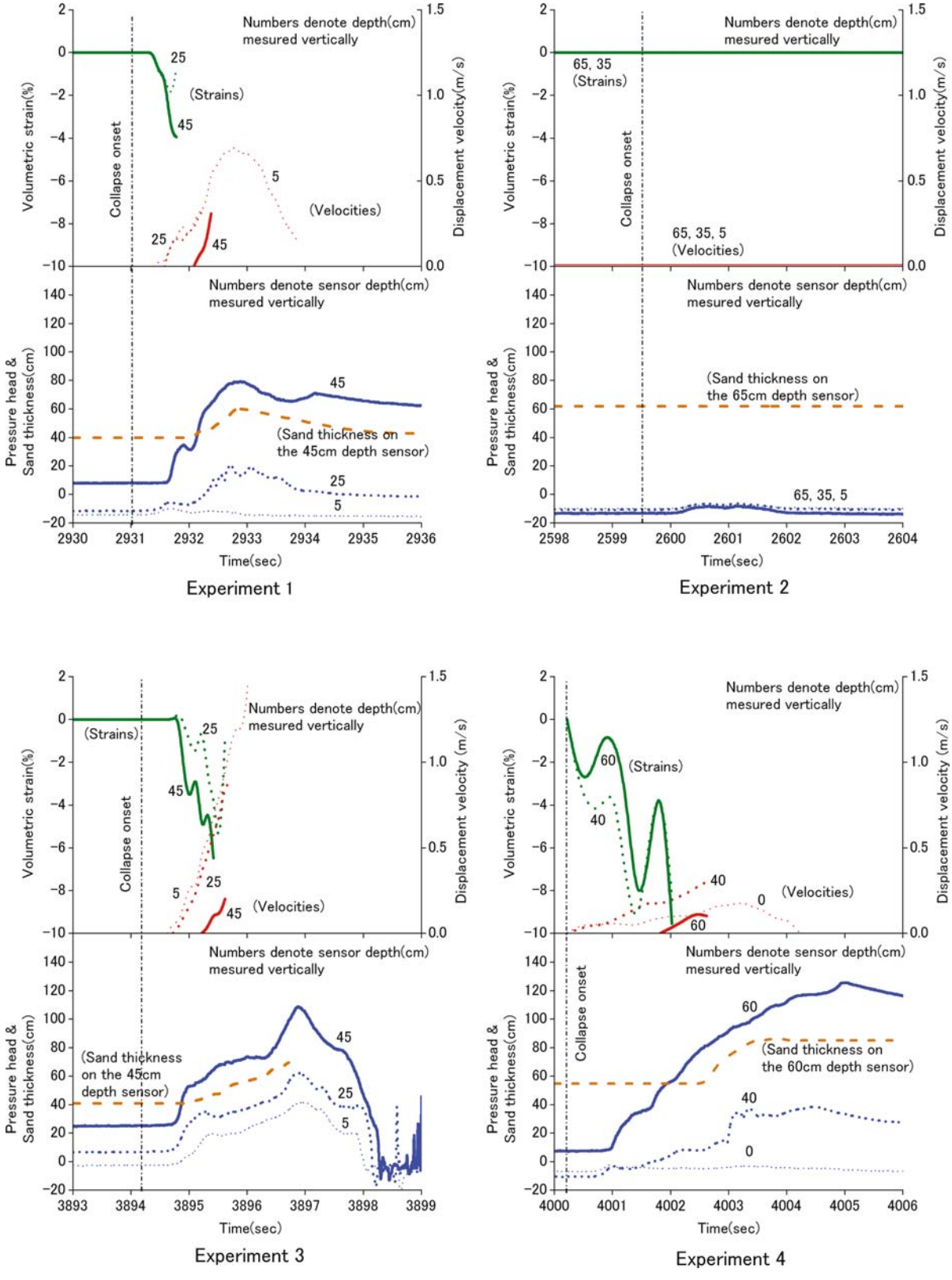

Fig. 15.9. The volumetric strain, thickness, pressure head and displacement velocity of sand layer at 3 m point from the lowest end of the flume in the case of Experiment 1 to 4

This mainly because that the void between sand particles absorbs a volumetric shrinkage in unsaturated condition.

3. Sections that suffered excess pore water pressure showed a positive correlation between the thickness of the overlying sand and pore water pressure. This is likely attributable to water pressure supporting the overlying load. This also means that a large-scale landslide reduces effective stress ratio on the shear plane, thus shows a gentle slope of compensation and long travel distance.

We then analyzed the relationship between the sand movement near the slip surface and change in pore water pressure in upper slope. Figure 15.10 shows the speed of soil movement, volumetric strain, pore water pressure, and change in sand layer thickness, all at 7 m from the lowest end of the flume, for Experiment 1 to 2. In both experiments, the slip surface was formed near the floor of the flume at 45 cm deep. Experiments 3 and 4 were not analyzed since there was no piezometer installed near the slip surface.

In Experiment 1, shearing and volumetric shrinkage around slip surface generated increase of pore water pressure, and the slope lost stability and collapsed entirely since the coefficient of friction was smaller than the inclination of the slope (2 931 s). The rapid changes in head value at the 45 cm-deep section were probably attributable to the noises caused by the roughness on the flume floor. But it maintained constant value in average (2 932 s). Besides, sand layer thickness decreased because of velocity inclination from slip surface to sand layer surface (2 931~2 932 s). There was no correlation between pressure head and sand layer thickness, and pressure head did not exceeded sand layer thickness. It is considered that the generation of the excess pore water pressure was locally and temporary. The gradual rise in pore water pressure during the late landslide movement was likely caused by the landslide mass colliding against the lower slope and increasing the thickness of the sand.

Experiment 2 tended to be similar to 1. The rise of water pressure was retarded in a volumetric shrinkage. It seems to be because measurement position of the water pressure has deviated with calculation area of the volumetric strain a little.

Our analyses showed:

1. The process of the fluidization in the collapse source progresses in three steps: the destruction of sand particle skeleton and volumetric compaction with shear, rise in pore water pressure, and rapid shearing around the slip surface, these steps occurred almost simultaneously.
2. With conversion to high speed shearing, the velocity gradient from slip surface to sand layer surface arises, and the sand layer thickness decreases.

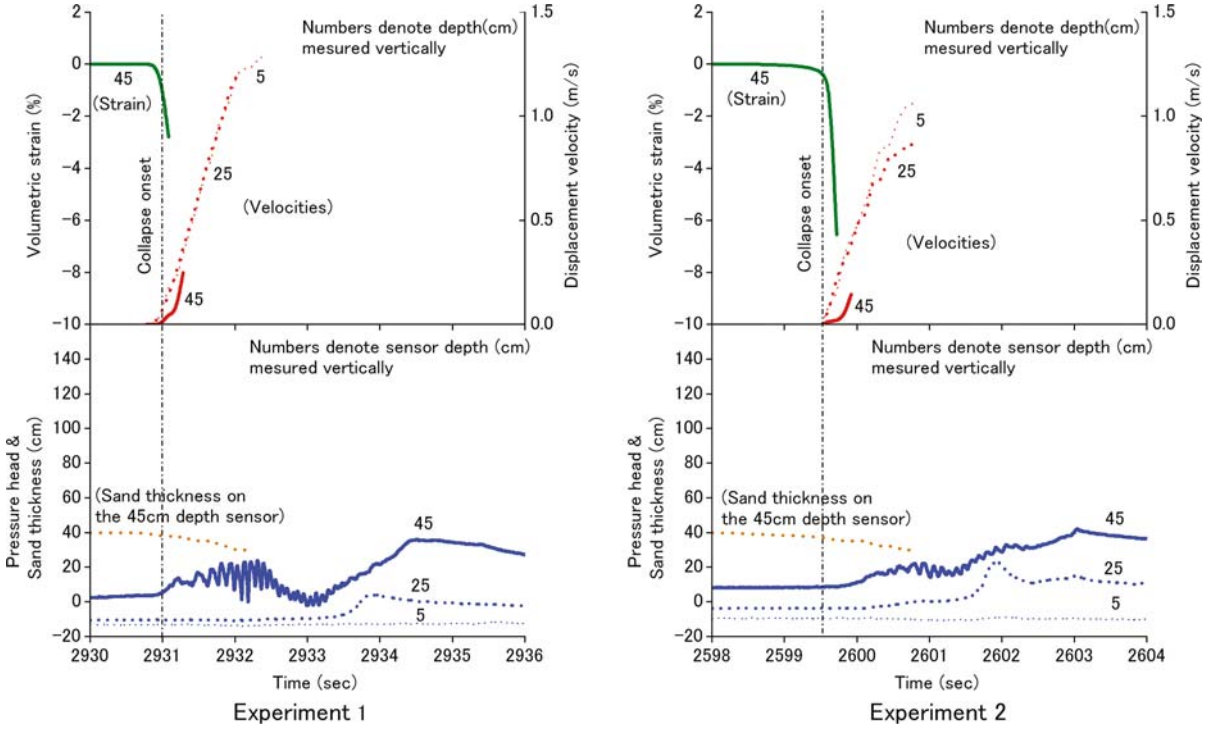

Fig. 15.10. The volumetric strain, thickness, pressure head and displacement velocity of sand layer at 7 m point from the lowest end of the flume in the case of Experiment 1 and 2

3. In high-speed shearing area at the collapse source, pressure head greatly did not rise, as it exceeded the sand layer thickness. This seems to be because that decreasing of thickness and disturbing of sand layer by high-speed shearring do not maintain the undrainage condition.

15.2.4.5 Landslide Fluidization Process by Flume Experiment

To clarify the fluidization process of heavy rain collapse demonstratively, we conducted landslide experiments using an almost real-size slope model equipped with a rainfall simulator. Both the movement and the pore water pressure of the sand layer were monitored throughout the experiment, from the start of spraying rain to the cessation of the landslide. Our experiments showed:

1. Landslide fluidization caused by undrained sudden loading of landslide mass undergoes three stages: compaction of the sand layer caused by the collapsed mass from upper stream, generation of excess pore water pressure in saturated soil sections, and induction of fast shearing. Besides, sections that suffered excess pore water pressure showed a positive correlation between the thickness of the overlying sand and pore water pressure. This is likely attributable to water pressure supporting the overlying load. This also means that a large-scale landslide reduces effective stress ratio on the shear plane, thus shows a gentle slope of compensation and long travel distance.
2. Landslide fluidization at the collapse source area undergoes also three stages: the volumetric compaction with shear, rise in pore water pressure in saturated zone, and rapid shearing around the slip surface, these steps occurred almost simultaneously. With conversion to high speed shearing, the velocity gradient from shear plane to sand layer surface arises, and the sand layer thickness decreases. The rise in pore water pressure is limited near the slip surface, and it does not rise as exceeding the sand layer thickness. This seems to be because that decreasing of thickness and disturbing of sand layer by high-speed shearing did not maintain the undrainage condition.

15.3 A Fluidized Landslide on Natural Slope Experiment

15.3.1 Experiment Site and Testing Procedure

The purpose of our experiment is to produce hopefully a fluidized landside on a natural slope by artificial rain fall. The test site was selected by two conditions: (*1*) to secure complete safety during the experiment, (*2*) to have a possibility producing a fluidized landslide. Then, a natural slope in the Koido National Forest at Mt. Kaba-san, Yamato village, 25 km north of Tsukuba-city, Ibaraki Prefecture, Japan was selected for the controlled experiment on landslide and possible fluidization in cooperation with the Forestry Agency of Japan.

The selected portion of hillslope (Fig. 15.11) was 30 meters long, with an average gradient of 33 degrees (maximum 35 degrees). The soil was 1 to 3 meters deep. A 5 m wide experimental slope was isolated from its surroundings by driving thin steel plates about 1 m deep into the soil. These plates prevented lateral diffusion of infiltrated rain water and cut the lateral tree root network that imparts resistance within the soil layer. The surface of the slope was covered by straw matting to prevent surface erosion and promote rainfall infiltration. Surface material on the slope consisted of fine weathered disintegrated granite sand, called "Masa" in Japan. Loamy soil blanketed the upper portion of the regolith to a depth of about 1 m; this soil mainly originated from tephra of Mt. Fuji, Mt. Akagi, and other volcanoes located west of Mt. Kaba-san.

Table 15.3. Examples of landslide experiments on natural slopes

References	Location	Volume $W \times L$	Excavation etc.	Water supply	Sensors	Fluidization
Oka (1972)	Ikuta, Kawasaki, Japan	500 m^3		Sprayed from fire hose		Yes
Yagi et al. (1985)	Matsuyama, Japan	10 × 25 m	Trench cut at upper and both sides	Rainfall simulator (sprayed on upper half slope)	Extensometer, Piezometer, Strain meter	Yes
Yamaguchi et al. (1989)	Yui, Shizuoka, Japan	10 × 30 m	Upper trench cut, Lower open cut	Supplied from upper trench	Extensometer, Piezometer, Inclinometer	No
Harp et al. (1990)	Utah, USA	1.6 × 1.3 m 2.0 × 2.2 m 3.2 × 4.0 m	Upper trench cut, Lower open cut	Supplied from upper trench	Extensometer, Piezometer	No

Artificial rain at the rate of 78 mm hr^{-1} was applied to the slope segment during the experiment by way of a rainfall simulator. The simulator consisted of a framework of steel pipes with 24 sprinkling nozzles arranged 2 m above the soil surface. Water for sprinkling was pumped from a dam constructed in a small creek at the base of the slope into 80 water storage tanks (1 m^3 for each) on the neighboring hillslope prior to the experiment.

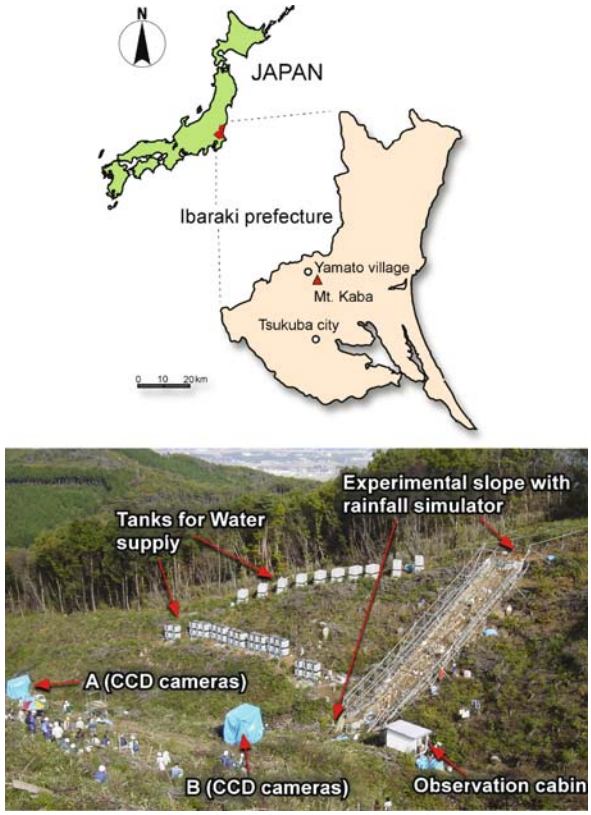

Fig. 15.11. View of the experiment site at Mt. Kaba-san

Soil-surface movement was measured by means of stereo photogrammetry. Five CCD video cameras (camera 1, 2, 3, 4, and 5) were placed on A, and another five (6, 7, 8, 9, and 10) on B in Fig. 15.11. The five stereo pairs of CCD video cameras were adjusted to film five parts of the experimental area from bottom to top. For image analysis, 40 white flat targets, 20 cm long×20 cm wide were distributed over the slope and nailed 20 cm deep. For three-dimensional stereo photogrammetry of the targets, *X*, *Y* and *Z* coordinates of eight control points (at least six for each camera) were obtained before photogrammetric analysis. The control points were 24 pieces of 15 cm diameter domed foam-polystyrene base points, attached to the steel pipes forming the framework of the sprinkling system. A schematic diagram of this measuring system is presented in Fig. 15.12. *Y*- and *Z*-axes were in the longitudinal plane of the experimental slope. The *Z*-axis was vertical and *Y*-axis horizontal. The *X*-axis was horizontal and normal to the *Y*-axis.

Film images were transmitted from the ten CCD video cameras to a 10-channel video time generator under the control of a video-synchronized distributor. Through the 10-channel video time generator, film images of the landslide movement with time-codes were recorded on hard-disk 1 to hard-disk 10, respectively. The 10-channel video time generator counted in time-steps of 0.01 s. The frequency of film imaging was 30 Hz. Calculation of target coordinates was carried out based on the DLT (Direct linear transformation) method. Each image was 480 pixels long×640 pixels wide, and one pixel represented about 1 cm×1 cm on the experimental slope. Trajectories of

Fig. 15.12.
Schematic of measuring system for stereo photogrammetry

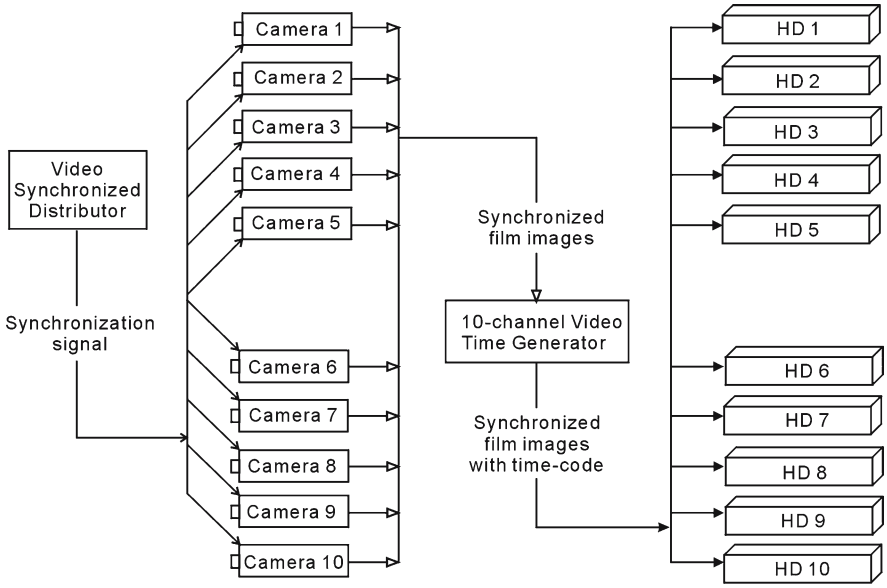

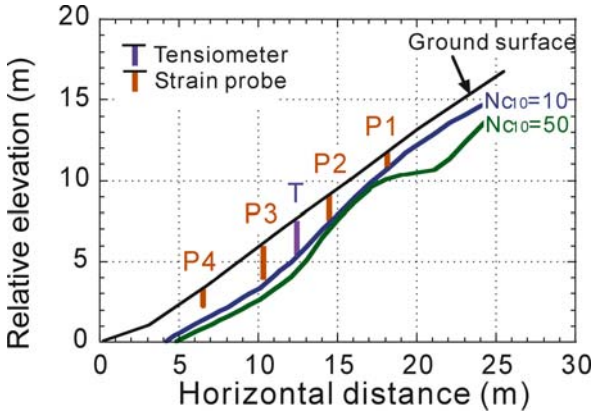

Fig. 15.13. Location of soil-strain probes and tensiometers on the slope. Soil depths are indicated by cone-penetrometer N_{c10} values

targets were detected using differences in brightness in image analysis. The white-coloured targets had a greater brightness than the other parts of the slope covered by straw matting. Coordinates of the targets were taken at the centres of pixel clusters with certain ranges of brightness.

To obtain information on the formation of the sliding surface, four soil-strain probes were inserted into the soil at P1, P2, P3, and P4, as shown in Fig. 15.13. Note that in Fig. 15.13, lines are drawn at the depths where values of $N_{c10} = 10$ and 50 were obtained by light weight cone-penetrometer testing (Noguchi et al. 1997). The N_{c10} values are the number of times it took to drop a weight (5 kg) from height of 50 cm to drive the cone 10 cm into the soil. These values defined the surface soil layer ($5 \geq N_{c10} \geq 0$) and total soil depth ($50 \geq N_{c10} \geq 0$), respectively. The strain probes were made by attaching strain gauges to both the front and back sides of cylindrical polyvinyl-chloride rods (diameter = 10 mm, 100 cm in length). The distance between each strain gauge was 10 cm. Each rod was coated by a waterproofing tube (Fig. 15.14). To measure the parts in which the sliding surface was expected to be deeper than 1 meter, two strain probes were connected to make a probe 2 m in length. The data acquisition rate was at 1/60 Hz and data were recorded on a data logger under PC control.

To measure saturation conditions within the soil, tensiometers with porous ceramic cups were set into the slope at T as shown in Fig. 15.13. Tenisiometer can measure negative pore water pressure in unsaturated soils and positive pore water pressure in saturated conditions. The data from respective sensors were transmitted through cables to the observation cabin, where they were monitored and recorded. The data acquisition interval for tensiometers was one minute

Several digital video cameras were placed in positions of safety on a hillslope facing the experimental slope to film the entire scene of the fluidized landslide.

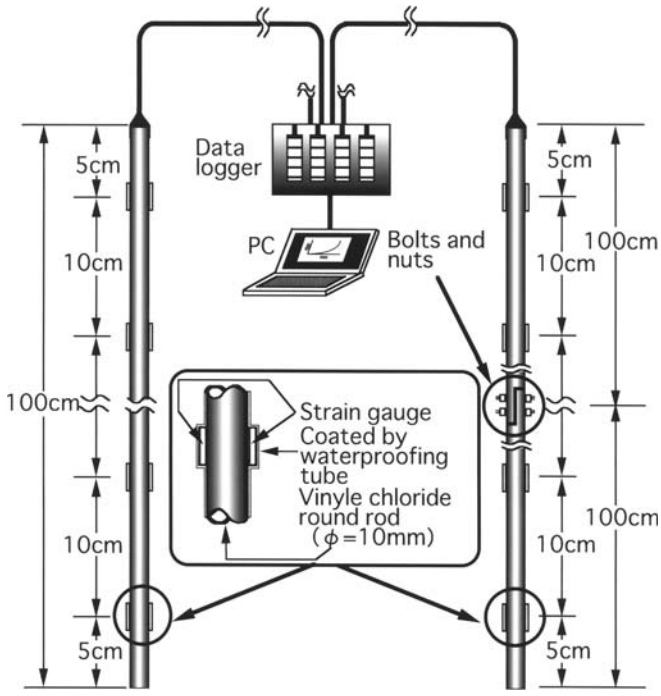

Fig. 15.14. Schematic of the strain probes

15.3.2 General Landslide Movement

On the 12 November 2003, artificial rainfall was given to the slope at a rainfall intensity of 78 mm hr^{-1} for four hours and a half until sunset. No slope movement was observed. The second experiment was conducted on 14 November 2003. Artificial rainfall was started from 9:13 at a rainfall intensity of 78 mm hr^{-1}, the slope deformation was detected from around 15:00, then a clear movement was observed to start at 16:03. The initiated landslide was a type of an expected fluidized landslide, the landslide mass rapidly moved and traveled long.

The cover of the tensiometer started to incline downslope at 24 627.5 s (410 min 27.5 s) after sprinkling commenced. We interpret this as indicating that slope failure initiated at 24 627.5 s. Some images from the digital video camera are presented in Fig. 15.15a–d. Figure 15.15a is at 24 628.5 s (one second after failure initiation), Fig. 15.15b at 24 629.5 s (two seconds), Fig. 15.15c at 24 630.5 s (three seconds), and Fig. 15.15d at 24 631.5 s (four seconds). As soil surface movement increased, a tension crack became visible at the head (Fig. 15.15a), and a compressive bulge resulting from downslope movement was observed 5 m above the base of the slope (Fig. 15.15b). The bulge enlarged (Fig. 15.15c) before the main landslide mass began to undulate and rapidly enter the stream (Fig. 15.15d). The compressive bulge was observed only in the left part of the landslide.

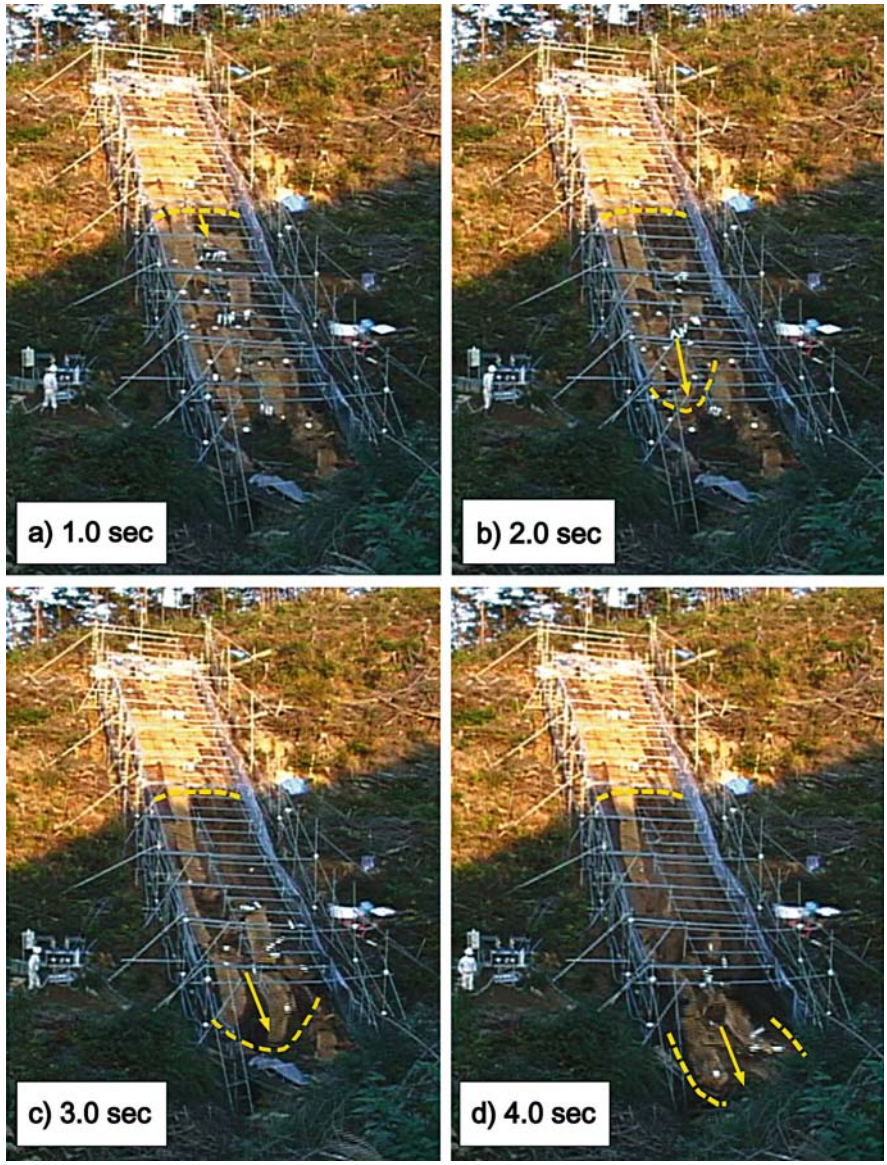

Fig. 15.15.
Views of the landslide fluidization between one second and four seconds after failure

Fig. 15.16. Views of the debris flow resulting from the landslide fluidization between five seconds and seven seconds after failure

Fig. 15.17. The landslide deposit one day after the experiment

Images at 24 632.5 s (five seconds after failure) and 24 634.5 s (seven seconds) are shown in Fig. 15.16a,b. Figure 15.16 presents the movement of liquefied landslide mass. The failed landslide mass had entered the stream and was about to collide with the confronting slope (Fig. 15.16a). After collision, the fluidized landslide turned to the right (Fig. 15.16b), changed into a debris flow, and traveled downstream for 10 seconds on a ~10 degree gradient, as much as 30 m. It took 17 seconds from the initiation of the landslide to the end of deposition. Figure 15.17 shows the landslide deposit one day after the experiment. The straw matting, the cover of the tensiometers, and the white-coloured targets were conveyed to the toe of the fluidized landslide.

15.3.3 Dynamic Movement of the Failed Landslide Mass

For stereo photogrammetry, imaging continued from the start of sprinkling until sunset, a duration of more than seven hours. However, the images in bright sunshine could not be analyzed, and motion of the targets was obtained from stereo photogrammetry only during failure initiation, and after slope failure had taken place. Data from 24 620 s (410 min 20 s) through 24 632 s (410 min 32 s) are shown. The arrangement of the targets on the failed landslide mass is shown in Fig. 15.18.

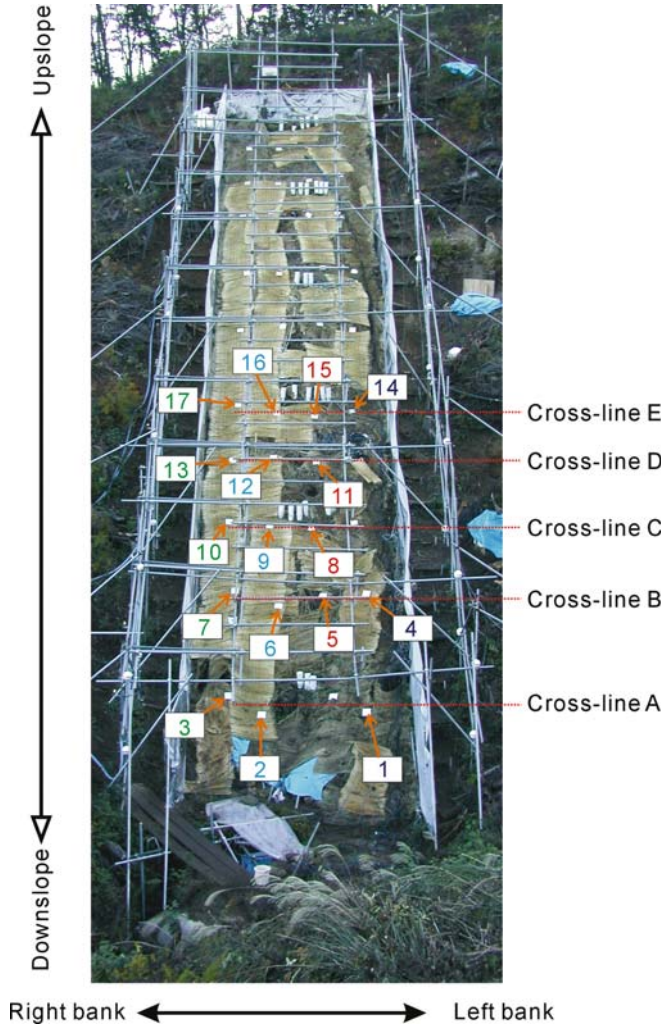

Fig. 15.18. Arrangement of targets for image analysis

Displacements of the targets in the *YZ*-plane are presented in Fig. 15.19. Targets on the cross-lines of C, D, and E, showed similar dynamic movement. From about 24 627.5 s (410 min 27.5 s), displacements were observable, and greatly increased in value from about 24 628.5 s. Although the available duration times for stereo photogrammetry differed for different targets, differences in the shapes of their motion curves were negligible. For targets on the cross-line B (targets 4 to 7), motions were very different: targets 6 and 7 which were nailed in the right hand bank of the experimental slope (left part of the experimental slope), showed rather similar behavior to that of targets 8 through 17. Target 5 however showed very small movement and target 4 showed no movement. Targets 1–3 on cross-line A did not move. This showed that parts in left hand bank (right side in the experimental slope) at cross-line B and parts around cross-line A neither failed nor slid, but remained stable.

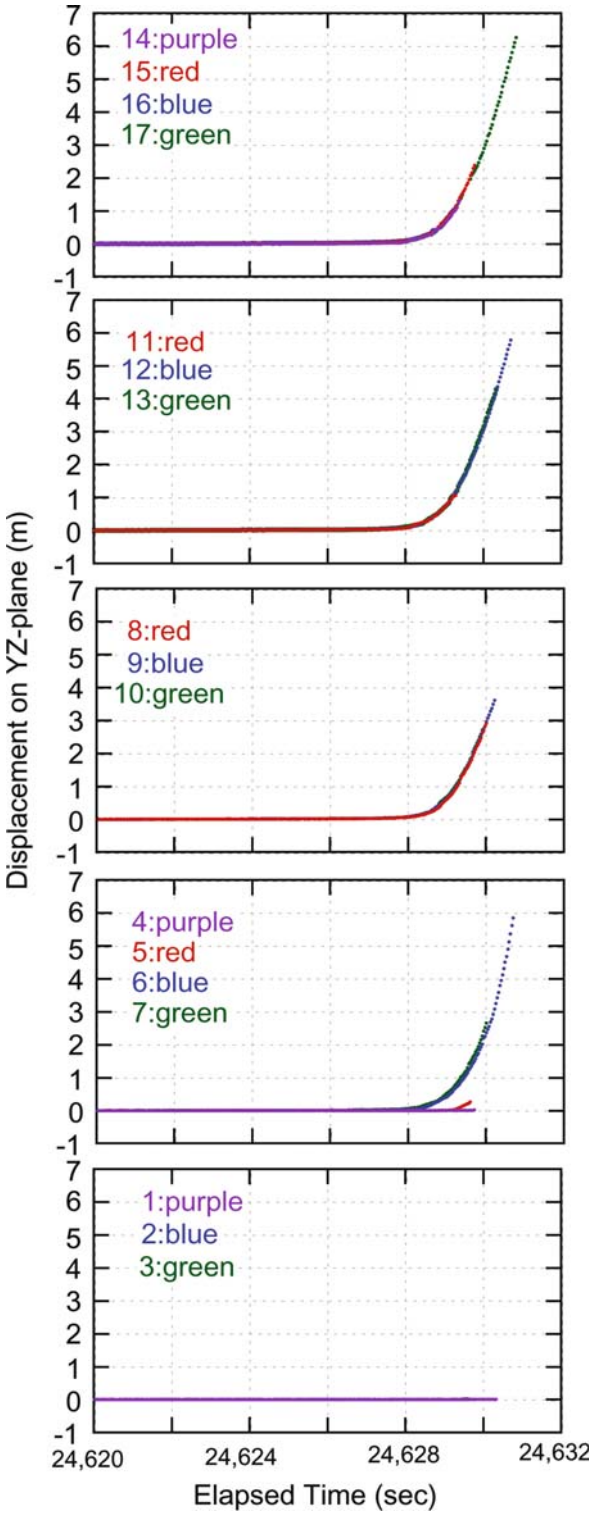

Fig. 15.19. Displacements of targets in the *YZ*-plane

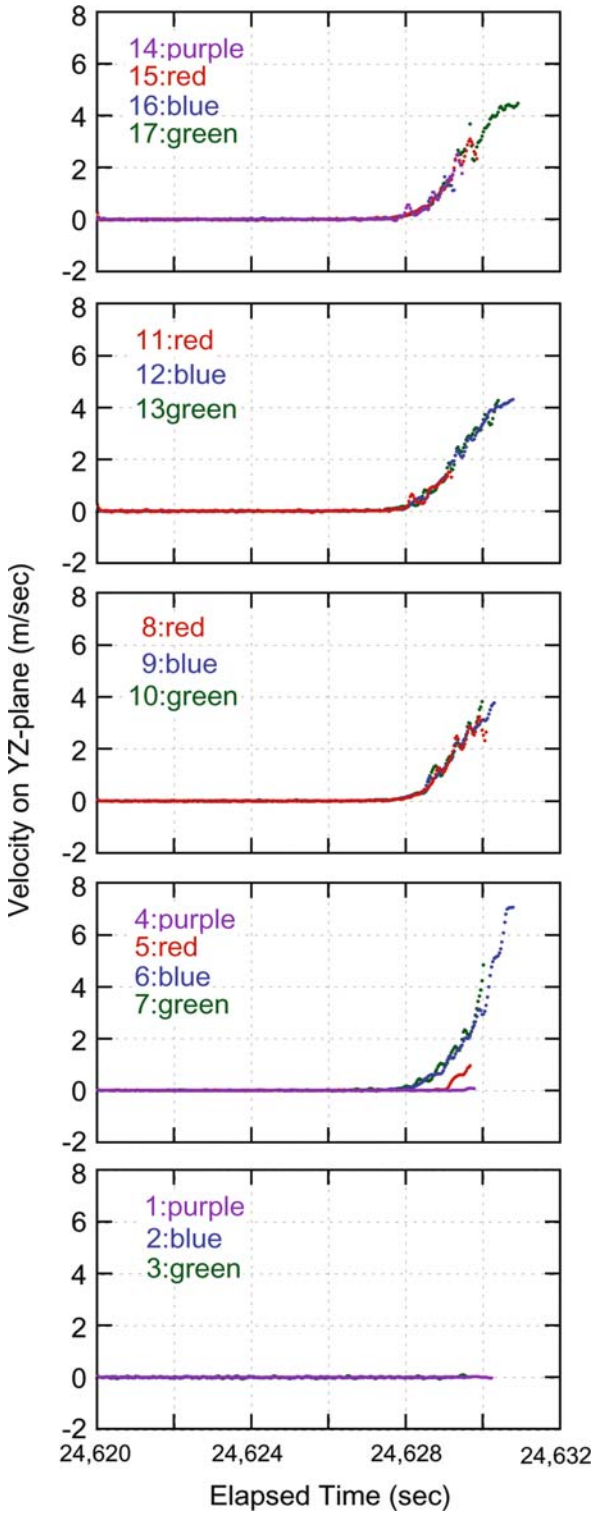

Fig. 15.20. Velocities of targets in *YZ*-plane

Velocities of targets in the *YZ*-plane are presented in Fig. 15.20. Since targets 1 through 4 did not move, their velocities were zero. Other targets increased their velocities after about 24 627.5 s, the time of failure initiation based on film images showing inclination of the cover of the tensiometer at this time. The target-velocity curves

in the *YZ*-plane confirmed the failure initiation time. Although the velocities of targets 5, 6, and 7 were different, the velocities of targets 8 through 17 during 24 628.5 to 24 630 s increased in proportion to time, and the shapes were similar to one another. Calculated average accelerations during this period were about 2 m s^{-2}. This value of acceleration in a sled model (Sassa 1988) on a 33 degree slope gives an apparent mobilized friction angle of approximately 22 degrees. The internal friction angle of weathered disintegrated granite sand is generally about 33 degrees, indicating a reduction of 11 degrees in apparent friction. This probably was due to excess pore pressure generated within the shear zone, followed by the landslide fluidization. The reason why targets 5 through 7 initially increased their velocities more slowly than targets 8 through 17 was that the former targets were located in the neighborhood of the break-out of the sliding surface (the foot). Hence they were in a zone of initial compression where the surface was observed to bulge upwards at the time of failure – see Fig. 15.22b.

Distances between longitudinally adjacent targets normalized by the initial distances between them before failure in the *YZ*-plane indicate longitudinal strain in the slope (Fig. 15.21, normalized distances along the south side are not presented). Longitudinal distances between cross-lines D & E (green color in Fig. 15.21) increase in value over time, whereas those between cross-lines A & B (purple), B & C (red), and C & D (blue) decrease. This indicates that tensional stresses were mobilized in the slope between cross-line D and E, whereas, compressive stresses occurred between cross-lines C and D, B and C, A and B. The normalized distance between 13–17 increased in value faster than those of between 11–15 and 12–16 (all of them were between cross-line D & E). We assume that expansive displacement was first mobilized around targets 13 and 17. While longitudinal surface strains between cross-lines D & E and C & D were small, strains between cross-lines A& B and B & C were large. Hence we assume that the slope between cross-line C and E likely failed and slid largely as a block. This interpretation is in general agreement with the velocity results (Fig. 15.20), in which targets 8 through 17 moved with similar velocities at any instant. The break-out of the sliding surface (the foot) appears to have been located above cross-line A. Note that the displacement behaviours of the targets on cross-line B (target 4, 5, 6, and 7) differ from all of the others (in Fig. 15.19). Targets 6 and 7 moved greatly, whereas target 4 and 5 showed little or no movement. Thus, the break-out of the sliding surface in the right hand bank (left part) of the experimental slope was likely between cross-line A and B, whereas, the one in the left hand bank (right part) was likely between cross-line B and C. Only one landslide was generated in this experiment, but the movement characteristics and stress conditions in the right and left hand banks were very different. The differences may be attributed to lateral heterogeneity in the soil on the slope.

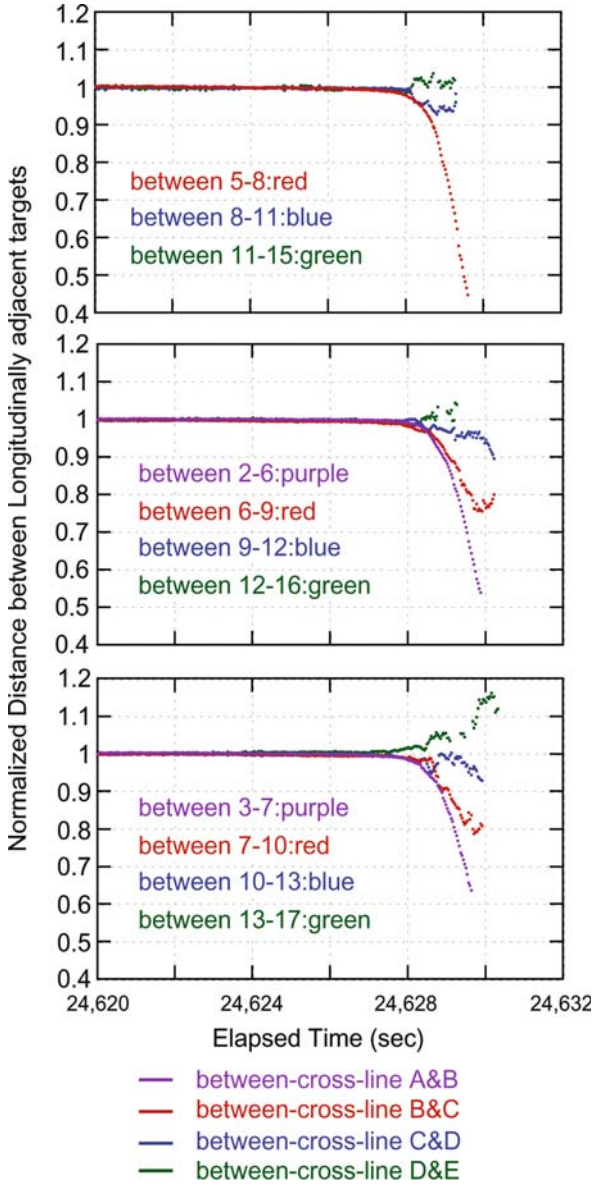

Fig. 15.21. Normalized distances between longitudinally adjacent targets in the *YZ*-plane

Snapshots of the three-dimensional movements of the targets are shown in Fig. 15.22. Figure 15.22a is 0.5 second before failure (24 627 s), Fig. 15.22b is two seconds after failure (24 629.5 s), and Fig. 15.22c is 3.5 seconds after failure (24 631 s). Targets 6 and 7, located just above the foot of the landslide, followed curved paths, which could not have been determined by conventional displacement measurement using extensometers. Figure 15.22 shows that the landslide mass overrode the slope around targets 2 and 3 and then moved rapidly into the stream at the foot of the experimental slope.

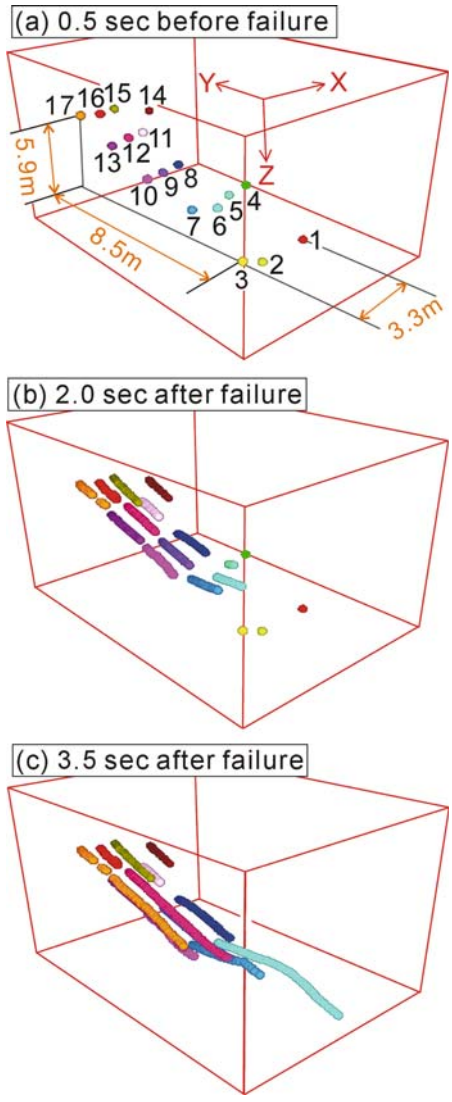

Fig. 15.22. Snapshots of the three-dimensional movements of the targets. **a** 0.5 second before failure (24627 seconds); **b** two seconds after failure (24629.5 seconds); **c** 3.5 seconds after failure (24631 seconds)

15.3.4 Sliding-surface Formation

When a sliding surface forms, soil above the sliding surface tends to move downslope, whereas soil below it remains stable. In this situation, a soil-strain gauge located above the sliding surface shows negative values, and the gauge below the sliding surface shows positive values (Fig. 15.23). Hence, if adjacent strain gauges show paired positive and negative values, we assume that the sliding surface has formed between them. Soil-strain probes at P1 and P2 were outside of the slope failure. Figure 15.24 shows the accumulation of soil strain during the experiment. The results from soil-strain probe P3 is shown in Fig. 15.24a, and for P4 in Fig. 15.24b. For the strain probe

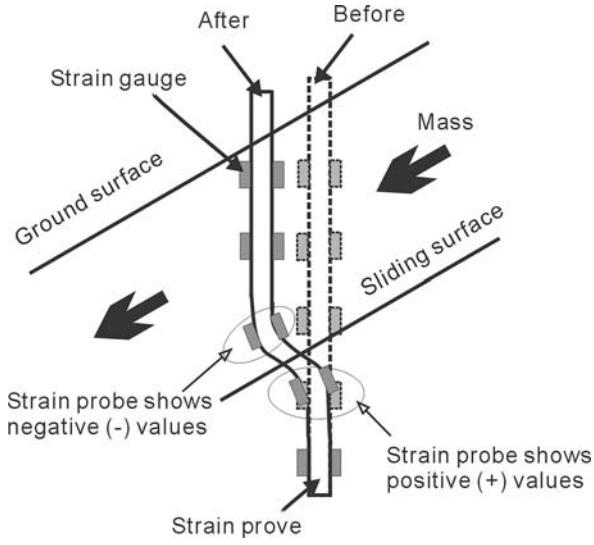

Fig. 15.23. Detection of soil strain by means of strain probes

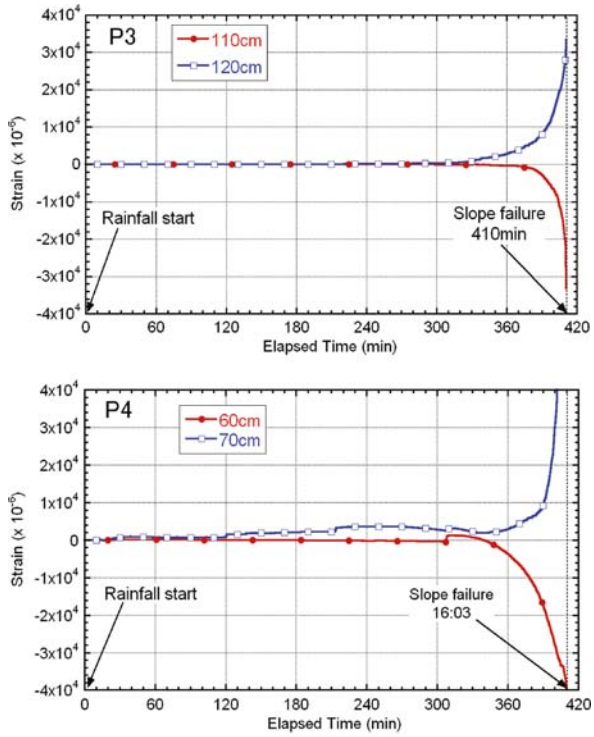

Fig. 15.24. Soil-strain accumulation curves (**a**) at P3 and (**b**) at P4

at P4 (Fig. 15.24b), positive values of strain were observed at a depth of 70 cm from about 20 minutes after sprinkling began, and negative strains at a depth of 60 cm. We interpret from the paired positive and negative values in Fig. 15.23, that the sliding surface formed between 60 cm and 70 cm depth. At failure (410 minutes), the accumulated strain at a depth of 70-cm was larger than 0.04, which

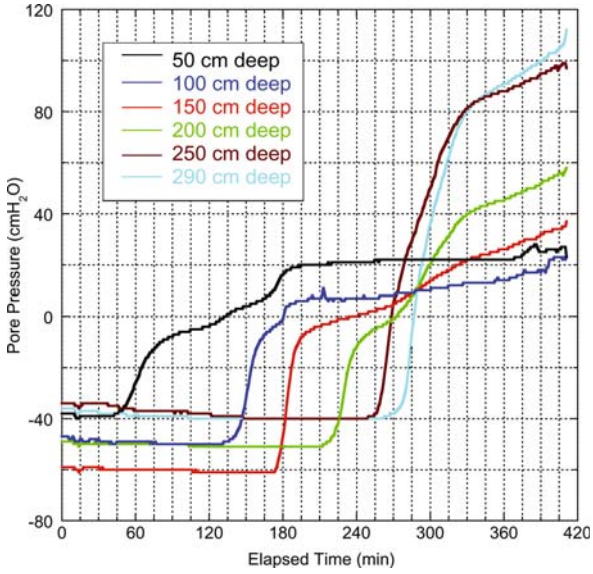

Fig. 15.25. Changes in soil-water pressure in tensiometers at *T*

was the capacity of the strain gauge. Similar results were obtained at P3 (Fig. 15.24a). Positive values of strain were observed at 120 cm depth from about 300 minutes and negative values at 110 cm depth, indicating a sliding surface between 110 cm and 120 cm depth. The depth of sliding at P3 was twice as deep as at P4.

Changes in pore water pressure including suction monitored by the tensiometers at T are presented in Fig. 15.25. The tensiometers at T were placed at depths of 50, 100, 150, 200, 250, and 290 cm. All tensiometers showed negative pore pressures at the start of sprinkling, indicating that the soils at all depths were unsaturated or partly saturated. When the wetting front passed, the tensiometers showed increases in pore pressure in sequence of the depths. At 410 min, when the failure took place, all of the tensiometers showed positive pore pressures. The pore pressure of the deepest tensiometer (290 cm) rapidly increased its values from about 290 min. This almost coincided with the time when the strain gauge at 110 cm depth in the strain probe at P3 started to show strain (Fig. 15.24a). Hence, it can be deduced that general slope instability increased from 290 min, before final failure at 410 min.

15.3.5 A Fluidized Landslide on Natural Slope by Artificial Rainfall

An experiment to induce a fluidized landslide by artificial rainfall was conducted on a natural slope at Mt. Kabasan in Yamato village, Ibaraki Prefecture, Japan. A landslide initiated 24 627.5 s (410 min 27.5 s) after the start of sprinkling at a rainfall intensity of 78 mm hr^{-1}. The landslide mass was 14 m long and 1.2 m deep (at maximum). It first slid, then fluidized, and changed into a debris flow. The travel distance was up to 50 m in 17 seconds. The apparent friction angle of the fluidized landslide was 16.7 degrees.

1. The entire landslide movement and subsequent debris-flow mobilization were successfully recorded by the digital video cameras, allowing qualitative interpretation of the shape of the landslide and definition of failure initiation and deposition times.
2. The soil-surface movements were measured by tracing the three-dimensional displacement of targets on the experimental slope using image analysis. Soil-surface movement of the failed landslide mass on the right and left banks were different. This may be attributed to heterogeneity in the composite soil on the slope.
3. Formation of the sliding surface was detected by soil-strain probes. Strain probes inserted in the middle or lower parts of the mass that failed showed a sliding surface at depths of between 110–120 cm and 60–70 cm, respectively. The tensiometer showed a rapid increase in pore-water pressure after about 290 min from the start of sprinkling. This almost coincided with the time when the strain was first observed on the sliding surface.

Acknowledgment

We acknowledge the help of Hiroshi Fukuoka, Ryo Sasaki, Sergio Lourenco, and Ivan Gratchev of Disaster Prevention Research Institute, Kyoto University, and Kotaro Makihara, Seishi Aihara and Yoshinori Yatabe of Chiba University. Also we wish to thank Hiromu Moriwaki, National Research Institute for Earth Science and Disaster Prevention for the advice for planning the field experiment. And also we appreciate the support of a number of the staff at Forestry and Forest Products Research Institute, especially to Yoshitsugu Takeuchi, Yukio Mashima, and Shozo Nakamura. We are indebted to Ibaraki Prefectural Government and Kanto Regional Forest Office for the permission to conduct the experiment in the Suigo-Tsukuba Quasi-National Park and Koido National Forest.

Flume experiments were conducted as part of the joint research for investigating the conditions of fluidization of landslide, by the Chubu Regional Forestry Office of Forestry Agency and Forestry and Forest Products Research Institute.

Landslide experiment on natural slope was a part of a project called APERIF (Areal Prediction of Earthquake and Rainfall Induced Rapid and Long-traveling Flow Phenomena), launched by the Special Coordinating Fund for Science and Technology of the Ministry of Education, Cultures, Sports, Science and Technology (MEXT) of Japan. In 2002, this project was approved as part of the International Programme on Landslides (IPL M101-APERITIF Project to the International Consortium on Landslides).

References

Bishop AW (1973) The stability of tips and spoil heaps. Q J Eng Geol 6:335–376

Committee of investigation for Gamahara-zawa debris flow damage in Dec. 6 (1997) The research report of investigation for Gamahara-zawa debris flow damage in Dec.6. J Jpn Soc Erosion Control Engng 50(3):89–94 (in Japanese)

Eckersley JD (1985) Flowslides in stockpiled coal. Eng Geol 22:13–22

Eckersley JD (1990) Instrumented laboratory flowslides. Géotechnique 40(3):489–502

Ellen SD, Fleming RW (1987) Mobilization of debris flows from soil slips, San Francisco Bay region, California. Geol Soc Am Rev Engng Geol 7:31–40

Fukuzono T (1985) A new method for predicting the failure time of a slope. In: Proceedings of IVth International Conference and Field Workshop on Landslides, Tokyo, 23–31 August, Japan Landslide Society, 1, pp 145–150

Harp EL, Wells WG, Sarmiento JG (1990) Pore pressure response during failure in soils. Geol Soc Am Bull 102:428–438

Hutchinson JN (1986) A sliding-consolidation model for flow slides. Can Geotech J 23:115–126

Ishihara K (1993) Liquefaction and flow failure during earthquakes. Géotechnique 43(3):349–451

Ishihara K, Okusa S, Oyagi N, Ischuk A (1990) Liquefaction-induced flowslide in the collapsible loess deposit in Soviet Tajik. Soils and Foundations 30(4):73–89

Iverson RM, LaHusen RG (1989) Dynamic pore-pressure fluctuations in rapidly shearing granular materials. Science 246:769–799

Iverson, RM, Reid ME, Iverson NR, LaHusen RG., Logan M, Mann JE, Brien DL (2000) Acute sensitivity of landslide rates to initial soil porosity. Science 290:513–516

Noguchi S, Abdul Rahim N, Zulkifli Y, Tani M, Sammori T (1997) Soil physical properties and preferential flow pathways in tropical rain forest, Bukit Tarek, Peninsular Malaysia. J Forest Res 2:125–132

Oka H (1972) Impacts by the "artificial landslide": re-examine the rage of nature. Kagaku Asahi, January issue, pp 152–153 (in Japanese)

Sassa K (1984) The mechanism starting liquefied landslides and debris flows. In: Proceedings of 4th International Symposium on Landslides, Toronto, June, 2, pp 349–354

Sassa K (1988) Motion of landslides and debris flows-prediction of hazard area. In: Report for Grant-in-Aid for Scientific Research by Japanese Ministry on Education, Science and Culture (Project No. 61480062), pp 4–52

Sassa K (1998) Mechanisms of landslide triggered debris flows. Environmental Forest Science. In: Proceedings of IUFRO Division 8 Conference, Kyoto, 19 – 23 October, pp 499–518

Sassa K (2000) Mechanism of flows in granular soils. In: Proceedings of the International Conference of Geotechnical and Geological Engineering, GEOENG2000, Melbourne, 1, pp 1671–1702

Sassa K, Fukuoka H, Wang G, Ishikawa N (2004) Undrained dynamic-loading ring-shear apparatus and its application to landslide dynamics. Landslides 1:7–19

Seed HB (1979) Soil liquefaction and cyclic mobility evaluation for level ground during earthquakes. J Geotech Eng-ASCE 105: 201–255

Seed HB, Lee KL (1966) Liquefaction of saturated sand during cyclic loading. J Geotech Eng-ASCE 92(CM6):105–134

Yagi N, Yatabe R, Enoki A (1985) Laboratory and field experiments on prediction method of occurring time of slope failure due to rainfall. Landslide (J Jpn Landslide Soc) 22(2):1–7 (in Japanese)

Yamaguchi I, Nishio K, Kawabe H, Shibano H, Iida C (1989) Initiation and fluidization of an artificial landslide. -Field experiment in Yui, Shizuoka Prefecture, Japan. Shinrin Kosoku (Areal Survey) 158:3–9 (in Japanese)

Yoshimi Y, Richart FE, Prakash S, Balkan DD, Ilyichev, VA (1977) Soil dynamics and its application to foundation engineering. In: Proceedings of the 9th International Conference on Soil Mechanics and Foundation Engineering, Tokyo, July, 2, pp 605–650